

5. Skyrmion and helical states in thin layers of magnets and liquid crystals *

PACS numbers: 75.70.-i, 75.50.Ee, 75.10.-b 75.30.Kz

I. INTRODUCTION

As shown in chapter 4, specific chiral interactions in *bulk* non - centrosymmetric helimagnets provide a unique mechanism for stabilization of the localized and modulated structures with fixed sense of the magnetization rotation in one (spirals) or in two (baby-skyrmion) dimensions. Twisted modulations of such a type arise as a result of the competition between the exchange stiffness and chiral interactions, whereas Zeeman energy in accordance with smaller energy contributions rules the thermodynamical stability of the corresponding modulated phases. Currently however, the scope of material science interest has been shifted to the *confined* artificial systems in which the structural inversion asymmetry of the surface gives rise to qualitatively new phenomena. The new aspects of the physics in reduced dimensions include Rashba effect^{1,2}, chiral Dzyaloshinskii-Moriya interactions^{3,4}, surface/interface induced anisotropy^{5,6}, and/or anchoring in liquid crystals. Understanding of these effects opens up the perspectives to create chiral architectures in nanosystems and put into practice control over them.

Surface-induced uniaxial anisotropy is a key factor that can influence chiral modulated states in magnetic nanosystems. Its interplay with volume energy contributions leads to the formation of specific axisymmetric distributions of the magnetization, spherulites, which exist as smooth static solitonic textures and are extended into the third direction in accordance with the modulating effect of the surfaces. As a starting point for investigations of this phenomenon I have calculated the equilibrium structures of skyrmions in a nanolayer with the induced uniaxial anisotropy for a case of "thick" layers when the induced magnetic anisotropy is strongly localized to the layer surfaces (a rigorous criterion of "thick" layer can be found in Ref.5. In this limiting case the induced anisotropy can be treated as a mere surface effect (according to Néel's theory of surface anisotropy⁶) and is included into the corresponding micromagnetic equations only through boundary conditions. In section III-V I give a comprehensive analysis of the spherulitic states in confined nanolayers.

Dipolar stray fields appearing on the surface of confined layers are another important factor having a sizable effect on modulated states. Due to the strong magnetodipole interaction chiral helices and skyrmion lattices can be significantly deformed. In section VI I address this practically unexplored problem of the interplay between short-range energy contributions stabilizing modulated phases, skyrmions and helices, and the long-range magnetostatic forces.

II. PHENOMENOLOGICAL MODEL OF MODULATED STATES IN THIN MAGNETIC FILMS

Generally the surface-induced anisotropy must be considered as inhomogeneously distributed through the volume of the nanosystem. However, the case with the induced anisotropy constrained to the surface region represents the practically most important situation. When the penetration length λ_s is much smaller than the characteristic sizes of the system, the surface-induced interactions influence the magnetization distributions only through the boundary conditions for the energy functional. In Refs. 5,7, for instance, the corresponding estimates led to $\lambda = 1.9\text{\AA}$ for Co/Au films and $\lambda = 26.4; 31.9\text{\AA}$ for Ni/Cu multilayer systems.

Therefore, in many practically important cases the magnetic energy of a nanosystem can be simplified by reducing to a sum of the volume ($w_v(\mathbf{r})$) and surface ($w_s(\mathbf{r})$) contributions:

$$W = \int_V w_v d\mathbf{r} + \int_S w_s d\mathbf{r}. \quad (1)$$

Then the equilibrium distributions of the magnetization $\mathbf{m}(\mathbf{r})$ are derived by solving the Euler equations for the volume functional $w_v(\mathbf{m})$ with the boundary conditions imposed by surface energy $w_s(\mathbf{r})$ (see e.g.^{3,4,6}).

In the present chapter I consider a magnetic nanolayer infinite in x - and y -directions and confined by parallel planar surfaces at $z = \pm T/2$. I consider a simplified model of a chiral ferromagnet with energy densities:

$$w_v = A(\text{grad}\mathbf{m})^2 - \mathbf{H} \cdot \mathbf{m}M - K_u(\mathbf{m} \cdot \mathbf{a})^2 + w_D, \quad (2)$$

$w_s = -K_s(\mathbf{m} \cdot \mathbf{s})^2$, A is a stiffness constant, \mathbf{H} is the applied magnetic field, $\mathbf{m} = \mathbf{M}/M$ is the unity vector along the magnetization ($M = |\mathbf{M}|$), $K_u > 0$ and $K_s > 0$ are constants of volume and surface induced uniaxial anisotropies correspondingly, unity vectors \mathbf{u} and \mathbf{s} define these "easy" magnetization directions. Chiral DM energy is composed

from antisymmetric invariants linear with respect to first spatial derivatives, so called Lifshitz invariants $\mathcal{L}_{ij}^{(k)} = m_i (\partial m_j / \partial x_k) - m_j (\partial m_i / \partial x_k)$. Particularly for cubic noncentrosymmetric magnets^{45,47}

$$w_D = D (\mathcal{L}_{yx}^{(z)} + \mathcal{L}_{xz}^{(y)} + \mathcal{L}_{zy}^{(x)}) = D \mathbf{m} \cdot \text{rot} \mathbf{m} \quad (3)$$

For uniaxial noncentrosymmetric ferromagnets DM functionals $w_D(\mathbf{m})$ are listed in²⁷.

Importantly, such a model allows to describe also thin layers of chiral nematic liquid crystals sandwiched between two glass plates. The possible distributions of the director $\mathbf{n}(\mathbf{r})$ in a bulk cholesteric liquid crystal placed in an electric field $\mathbf{E} = E\mathbf{e}$ are determined by the minimization of the Frank free energy^{8,9}:

$$f_v = \frac{K_1}{2} (\text{div} \mathbf{n})^2 + \frac{K_2}{2} (\mathbf{n} \cdot \text{rot} \mathbf{n} - q_0)^2 + \frac{K_3}{2} (\mathbf{n} \times \text{rot} \mathbf{n})^2 - \frac{\varepsilon_0}{2} (\mathbf{n} \cdot \mathbf{E})^2. \quad (4)$$

Here, K_i ($i = 1, 2, 3$) and q_0 are elastic constants; ε_a is the dielectric anisotropic constant (we consider only materials with $\varepsilon_a > 0$); $p = 2\pi/|q_0|$ determines the pitch of a helical structure in the ground state (at $E = 0$). For the one elastic constant approximation, $K_1 = K_2 = K_3 = K$, the Frank energy density (4) can be reduced to the form:

$$f_v = K(\text{grad} \mathbf{n})^2 + 2Kq_0 \mathbf{n} \cdot \text{rot} \mathbf{n} - \varepsilon_0 E^2 (\mathbf{n} \cdot \mathbf{e})^2. \quad (5)$$

For $\mathbf{H} = 0$ the energy density w_v coincides functionally with $f_v(\mathbf{n})$ (Eq. 5). This allows to investigate skyrmionic states in chiral ferromagnets and liquid crystals within a common mathematical framework. The surface energy w_s for liquid crystals (Eq. (2)) describes a homeotropic anchoring of glass surfaces with $K_s > 0$ ⁹. In the experiments with liquid crystals, such glass surfaces confine a thin layer of a liquid crystal and anchor the molecules perpendicularly to the surfaces. Phenomenological model (Eq. (5)) allows to obtain continuous distributions of the director \mathbf{n} for liquid crystals.

III. ISOLATED SKYRMIONIC STATES

To investigate the structure of isolated skyrmions in thin magnetic layers one has to introduce cylindrical coordinates for the spatial variable $\mathbf{r} = (r, \phi, z)$, and the spherical coordinates for the order parameters \mathbf{m} and \mathbf{n} : $\mathbf{m}, \mathbf{n} = (\sin \theta \cos \psi, \sin \theta \sin \psi, \cos \theta)$. On the contrary to the isolated skyrmions in bulk systems which are characterized by the dependence $\theta = \theta(r)$ in the cross-section of a skyrmion filament and are homogeneously extended into the third direction (z), the localized skyrmions in confined media are solutions of the following boundary value problem with $\theta = \theta(r, z)$:

$$\begin{aligned} \theta_{ZZ} + \theta_{\rho\rho} + \frac{\theta_\rho}{\rho} - \frac{\sin \theta \cos \theta}{\rho^2} - \frac{\sin^2 \theta}{\rho} - \gamma \sin 2\theta + h \sin \theta &= 0, \\ (\theta_Z + \beta \sin \theta \cos \theta)|_{Z=\pm t/2} &= 0, \\ \theta(0, Z) = \pi, \theta(\infty, Z) &= 0. \end{aligned} \quad (6)$$

Skyrmionic strings in such systems are distorted into specific 3D textures in accordance with the anchoring effect of the surfaces, but the topology remains the same¹⁰.

In Eq. (6) I introduced the new length scales for magnets:

$$\rho_0 = \frac{A}{D} \quad (7)$$

and liquid crystals

$$\rho_0 = \frac{1}{2q_0}. \quad (8)$$

Then $\rho = r/\rho_0, Z = z/\rho_0$. Four control parameters in Eq. (6), γ, h, β , and t , are expressed as combinations of material parameters of the model functional (2) and (5). For magnetic layers:

$$\gamma = \frac{AK_u}{D^2}, h = \frac{HM_s A}{D^2}, \beta = \frac{K_s}{D}, t = \frac{TD}{A}, \quad (9)$$

For liquid crystals:

$$\gamma = \frac{\varepsilon \varepsilon_0 E^2}{K q_0^2}, h = 0, \beta = \frac{K_s}{2K q_0}, t = 2T q_0. \quad (10)$$

Invariance of Eq. (6) under a scaling transformation:

$$t \rightarrow kt, \quad \gamma \rightarrow \gamma k^2, \quad h \rightarrow hk^2, \quad \beta \rightarrow \beta k. \quad (11)$$

allows to investigate solutions of Eq. (6) for a fixed reduced layer thickness t ($t=1$ in the present chapter). For the liquid crystals it is convenient to redefine anisotropy parameter γ and to write it in the units of \varkappa :

$$\gamma = \frac{\pi^2}{16\varkappa^2}, \quad \varkappa = \frac{E_0}{E}, \quad E_0 = \pi q_0 \sqrt{\frac{K}{4\varepsilon_0}}. \quad (12)$$

The critical field E_0^{10} marks the crossover between localized and modulated skyrmion states for bulk chiral helimagnets.

Boundary value problem (2) has been solved by a standard finite-difference method with discretization on rectangular grids with adjustable grid spacings. As initial guess for the iterative procedure according to Seidel method with Chebishev acceleration¹¹ I used the known solutions of Eq. (2) for bulk chiral systems¹², i.e. I started from the solutions with $\beta = 0$.

Solutions for isolated skyrmions may be represented as a set of profiles $\theta(\rho)$ for fixed coordinates Z . The profiles are strongly modified by the anchoring β from bell-like type in the center of the layer to arrow-like at the surface (blue lines in Fig. 1 (a)). The thickness-dependent radii $R(Z)$ for each angular profile $\theta(\rho)$ are defined as shown by red tangent lines in Fig. 1 (a), i.e. according to the Lilley definition. The function $R(Z)$ reproduces the convex shape of solutions with the largest value in the center of the layer ($Z = 0$) and the smallest value corresponding to the layer surfaces ($Z = \pm t/2$) (Fig. 1 (a), inset, and (b)-(e)). With increasing anchoring parameter β angular profiles $\theta(\rho)$ near the surfaces become strongly localized (Fig. 1 (b)) with the characteristic sizes comparable to the molecular length; in this case the elastic approach of Eq. (6) is inapplicable, and the isolated skyrmions collapse into the homogeneous state.

The influence of the surface anchoring may lead not only to the compression of ideally cylindrical filament into convex-shaped spherulite, but also to the specific skyrmionic states with "necks" when the minimal value of $R(Z)$ is reached not at the surface of the layer, but at some coordinate Z in the volume (Fig. 1 (c)). Such a peculiar shape of an isolated spherulite is a result of complex interplay between surface and volume energy contributions. It cannot be an artefact of the proposed method to define the function $R(Z)$ since the lines with constant angle θ show the same behaviour near the surface (see inset in Fig. 1 (a)).

The decrease of the film thickness t results in the same effects as increase of the anchoring parameter β (Fig. 1 (d), (e)) as it can be concluded from the equation (11) of the scale transformation. The set of profiles $R(Z)$ for the fixed value of anchoring parameter $\beta = 3$ and variable thicknesses t of the layer displays the change of the spherulite shape from that with "necks" for thin layers to the convex shape for thick films (Fig. 1 (d), (e)).

Still for the wide range of control parameters all angular profiles $\theta(\rho)$ are of arrow-like type squeezed along the sample thickness by anchoring. Such a type of angular profiles permits the use of the ansatz¹⁰:

$$\theta(\rho, Z) = \pi \frac{\rho}{R(Z)}. \quad (13)$$

The function $R(Z)$ describes the compression of angular profile $\theta(\rho)$ for $R > 1$ and its expansion with $R < 1$. Integrating (6) with the ansatz (13) with respect to ρ , results in

$$\int_{-t/2}^{t/2} \left[I_0 \left(\frac{dR}{dZ} \right)^2 + I_1 R^2 \left(\frac{\pi^2}{16\varkappa^2} \right) - I_2 R - I_3 h R^2 \right] dZ \quad (14)$$

where

$$\begin{aligned} I_0 &= \int_0^1 t^3 \left(\frac{d\theta}{dt} \right)^2 dt = \frac{\pi^2}{4}, \quad I_1 = \int_0^1 t \sin^2 \theta dt = \frac{1}{4}, \\ I_2 &= \int_0^1 t \left(\frac{d\theta}{dt} \right) dt = \frac{\pi}{2}, \quad I_3 = \int_0^1 \left(\frac{t}{2} \right) \cos(\theta) dt = -\frac{1}{\pi^2} \end{aligned} \quad (15)$$

The Euler equation for the functional (14) with the boundary conditions

$$\left(\frac{dR}{dZ} \right)_{Z=\pm t/2} = R(Z) \beta \frac{I_1}{I_0} \quad (16)$$

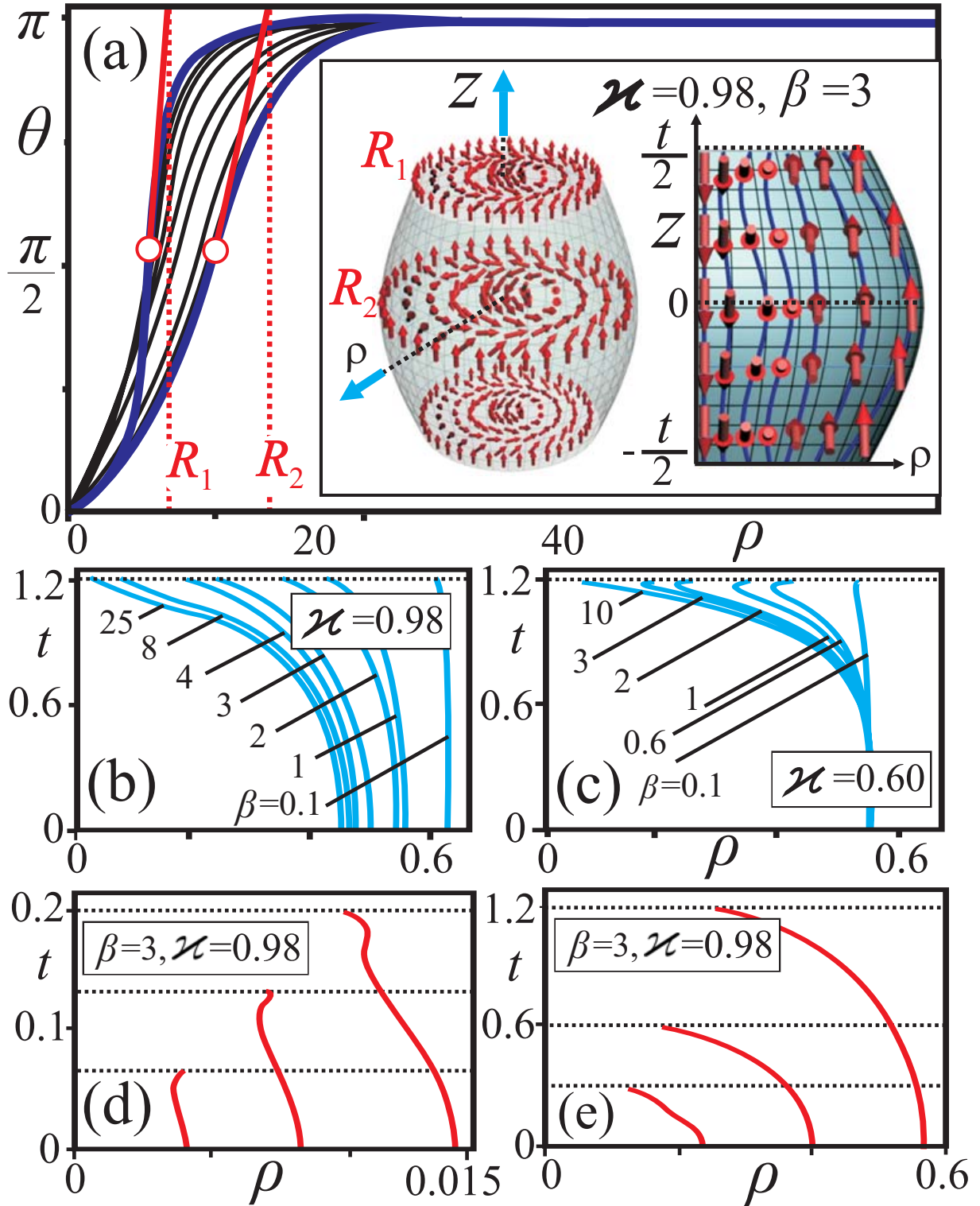


FIG. 1: (a) Equilibrium solutions of isolated spherulitic domains, shown as a set of profiles $\theta(\rho)$ for fixed coordinate Z through the layer. Bold blue lines mark the profiles at the surface and in the center of the layer. Inset schematically displays the distribution of the order parameter vector field with $\psi = \varphi - \pi/2$. The effect of anchoring is imaged by its influence on the boundary surface of the spherulite as shown in (a) by red lines for each angular profile: (b), (c) represent shapes of the localized spherulites for different values of surface anchoring β ; (d), (e) - for different film thicknesses t .

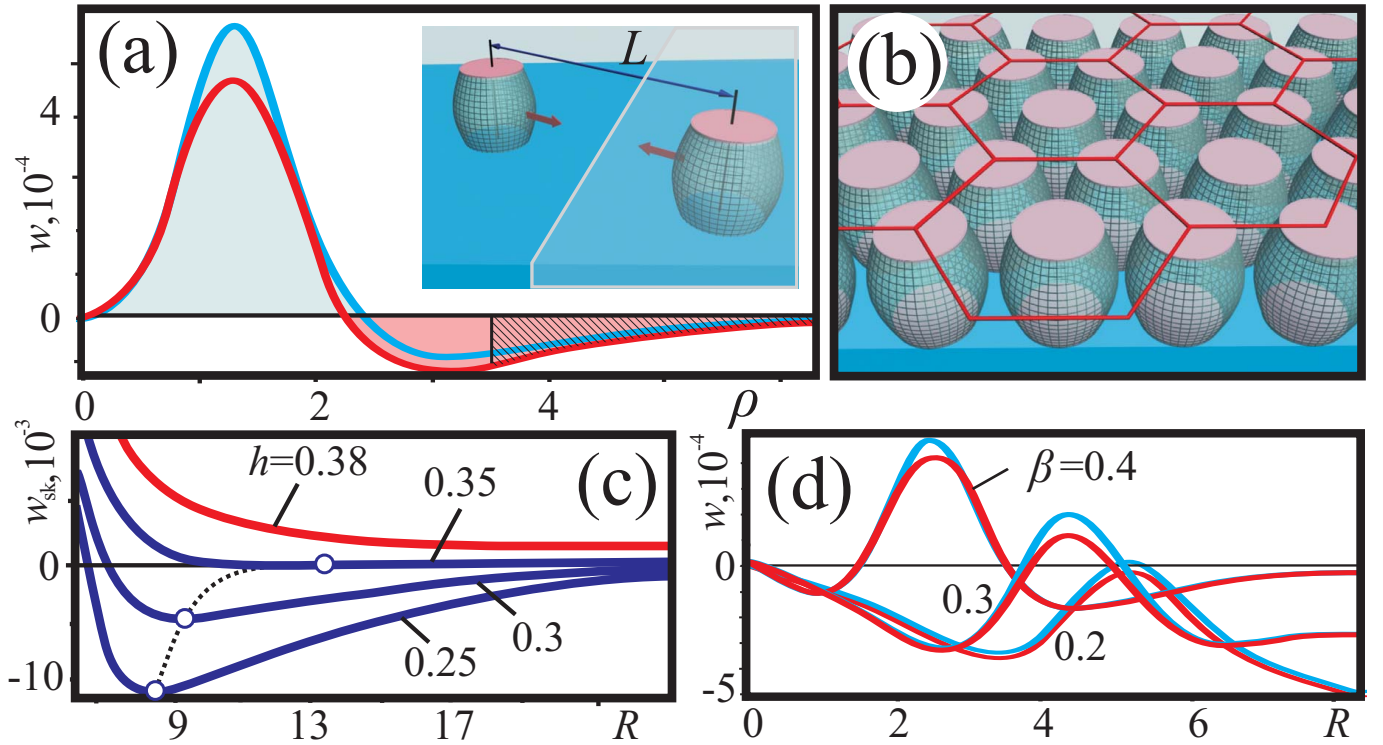


FIG. 2: Distribution of energy density in the isolated skyrmion state ($\beta = 0.5$) (a) and in the skyrmion lattice ($\beta = 0.2$) (d) for the profiles $\theta(\rho)$ at the surface (blue line) and in the central film plane (red line) ($\varkappa = 3, h = 0$); (b) schematic representation of the hexagonal skyrmion lattice in the circular cell approximation; (c) dependence of the skyrmion energy on the radius of lattice cell R for different values of the applied magnetic field ($\varkappa = 3, \beta = 0.1$). Above the threshold field (red line) only isolated skyrmions can exist.

has an analytical solution¹⁰:

$$R(Z) = \frac{1}{\pi A} \left(1 - \frac{\beta \cosh(Z\sqrt{A})}{\beta \cosh(\frac{t\sqrt{A}}{2}) + \pi^2 \sqrt{A} \sinh(\frac{t\sqrt{A}}{2})} \right), \quad A = \frac{1}{16\varkappa^2} + \frac{4h}{\pi^4}. \quad (17)$$

Considered analytical approach for arrow-like angular profiles describes numerically obtained solutions with a good accuracy, and can be generally applied for other appropriately chosen initial functions $\theta(\rho/R(z))$.

IV. CONDENSATION OF REPULSIVE SKYRMIONS INTO A LATTICE

In the *bulk* helimagnets the inter-skyrmion interaction is known to be repulsive and screened at large distances L . In thin confined layers the standard interaction of skyrmions is modified, and related to the exponential decay of the polar angle. The solution of the linearized Euler equation (6) for $\rho \rightarrow \infty$ has the asymptotic decay with

$$\theta(\rho, Z) \propto \cos(\lambda Z) \exp(-\alpha\rho). \quad (18)$$

Here, $\alpha = (\pi/4\varkappa)^2 - h + \lambda^2$, and λ are the roots of the transcendental equation, $\lambda \tan \lambda Z = \beta$ (Fig. 2 (a), inset). The energy density underlying such a slow rotation is negative and depends on the distance from the center of the layer. In Fig. 2 (a) I plotted the energy density distribution in the profile at the surface (blue line) and in the center of the layer (red line). The interaction energy of two vortices has the expression:

$$U(L, \beta) = \sqrt{\frac{2\pi L}{\alpha^3}} \exp(-\alpha L). \quad (19)$$

The parameter λ due to the anchoring effect of the surfaces modifies this inter-skyrmion potential in comparison with the volume case. The lattice will be established from isolated skyrmions when the DM energy contribution

(red-shaded area of energy distribution $w_{sk}(\rho)$, Fig. 2 (a)) of *all* profiles $\theta(\rho, Z)$ outweighs the exchange energy contribution (blue-shaded area). Since the exchange part of the energy density is much larger for the surface profiles $\theta(\rho, \pm t/2)$ (blue line in Fig. 2 (a)), the field of lattice formation will be smaller for larger values of parameter β (see, for instance, the second plot in Fig. 3 (d), \varkappa here is fixed). This explains the shape of the lability surface for the lattice of spherulites in Fig. 3 (a). For Skyrmionic states in the lattice I used the circular-cell approximation¹³ and solved Eq. (2) with boundary conditions $\theta(0, Z) = \pi, \theta(R(Z)) = 0$ (Fig. 2 (b)).

V. SKYRMION LATTICES VERSUS HELICOIDS. PHASE DIAGRAM OF SOLUTIONS

Alternative to the two-dimensional skyrmion state is the one-dimensional helicoid (Fig.3 (a), inset) with propagation vector along Y -axis, parallel to the surfaces. Angle θ of the magnetization with respect to Z axis in the helicoid can be obtained from the Euler equation with boundary conditions:

$$\begin{aligned} \theta_{ZZ} + \theta_{YY} - \gamma \sin \theta \cos \theta &= 0, \\ \theta(0) = \pi, \theta(p) &= 0, \\ \left(\frac{\partial \theta}{\partial Z} + \beta \sin \theta \cos \theta\right)|_{Z=\pm t/2} &= 0 \end{aligned} \quad (20)$$

where p is a period of the helicoid.

In the distorted helicoid propagating in the magnetic layer, angle θ is a function of two coordinates, Y and Z . This distinguishes the solutions $\theta(Y, Z)$ from those considered in chapter 4 with the dependence of the angle only on one spatial coordinate¹², $\theta = \theta(Y)$. In the plane XZ (see inset in Fig. 3 (a)) the solutions for helicoids have convex shape as it was noted also for spherulites. I have plotted the dependences $\theta = \theta(Z)$ in equidistant planes with fixed coordinate Y (thin black lines in Fig. 3 (b)). Such profiles have the most distorted shape in the vicinity of the point $Y = p/2$. Note that profiles for $Y = p/2$ are straight lines with $\theta = \pi/2$: the magnetization is balanced by the two anchoring surface planes. Dependence of the angle θ along coordinate Y is also strongly distorted by the anchoring effect of the surfaces: the order parameters \mathbf{m} (or \mathbf{n}) point up ($\theta = 0$) and down ($\theta = \pi$) in the wide regions (domains) and rotate rapidly in the interstitial regions (domain walls). Such a behavior of the spiral state may be also deduced from the densest localization of lines $\theta(Z)$ in the vicinity of $\theta = 0; \pi$ (thin black lines in Fig. 3 (b)).

The distribution of the energy density in the helicoid along the propagation direction Y is plotted in Fig. 3 (b) for the profiles at the surface $\theta(Y, t/2)$ (blue line) and in the center of the layer $\theta(Y, 0)$ (red line). The largest loss of the rotational energy occurs for the planes with $\theta = \pi/2$ (Fig.3 (b)).

On the phase diagram the regions of modulated skyrmion matter and helicoidal state are bounded by the surfaces with red and black lability lines, respectively (Fig. 3 (a)). Corresponding two-dimensional cuts of this three-dimensional phase diagram are shown in Fig. 3 (d). For $h = 0$ (i.e. in the plane (\varkappa, β)) the energy density of the helicoid is always lower than that for skyrmion lattice (Fig. 3 (c)), i.e. skyrmions are metastable states with respect to helicoids for all possible values of the anchoring parameter β . The region of the thermodynamical stability of the helical state is marked by blue color in Fig. 3 (d). According to the phase diagram of Fig. 3 (d), increasing parameter β (for fixed value of \varkappa) leads to the suppression of skyrmions (red line) for much lower values than the suppression of helical states (black line). If the skyrmion lattice as metastable state has been formed for $\beta = 0$, then on the lability (black) line it releases free isolated skyrmions. But since the helicoids are the global minimum of the system above the lability line of the skyrmion lattice, the isolated skyrmions must undergo elongation into the helices.

For $\varkappa \rightarrow \infty$ (meaning zero uniaxial anisotropy¹⁴), i.e. on the plane (β, h) (Fig. 3 (d)), the thermodynamical stability of skyrmions can be achieved in the applied magnetic field only for relatively small values of the anchoring parameter β - in the triangular region marked by red color in Fig. 3 (d). For values of β larger than some threshold β_{th} (Fig. 3 (d)), the helicoids are the thermodynamically stable state. On the basis of competing Zeeman energy and surface-induced uniaxial anisotropy the anchoring can be classified as weak (favouring skyrmion lattice in the field for $\beta < \beta_{th}$), intermediate (favouring helical state in zero and the applied magnetic field for $\beta_{th} < \beta < \beta_0$), and strong (only isolated domain walls and localized skyrmions can exist, $\beta > \beta_0$).

VI. MAGNETOSTATIC PROBLEM FOR ISOLATED SKYRMIONS

In previous sections I discussed characteristic features of modulated states arising as a result of competing internal short-range interactions (as the exchange interactions, the Dzyaloshinskii-Moriya coupling, different types of intrinsic and induced magnetic anisotropy) and ignored the effects imposed by magnetodipole forces. In many magnetic nanostructures this assumption is justified by weakness of stray field effects as compared to the internal magnetic

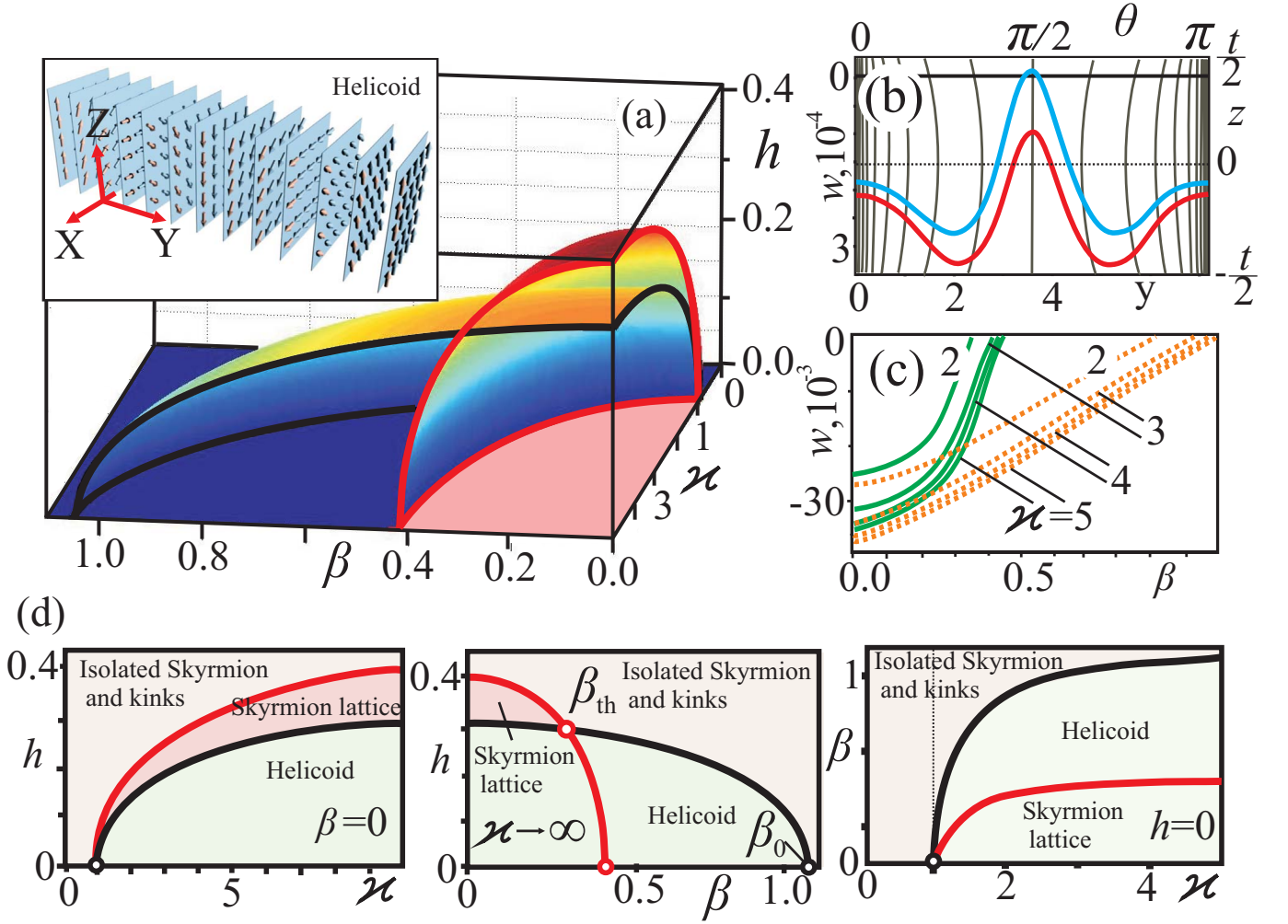


FIG. 3: (a) Phase diagram of solutions in the space of control parameters (χ, β, h) . Surfaces with red and black lines bound the regions of skyrmion lattice and helical state stability, respectively. (b) Distribution of the energy density in the helicoid ($\beta = 0.5$) for the profiles $\theta(Y)$ (see inset in (a) for schematic representation of distorted helicoid) at the surface (blue line) and in the central film plane (red line) ($\chi = 3, h = 0$); thin black lines show the dependences $\theta(Z)$ in equidistant planes ZX . (c) Energy dependence of equilibrium skyrmion lattice (green lines) and spiral state (dotted orange lines) on the changed parameter of surface anchoring β ($h = 0$). (d) The two-dimensional cuts of the three-dimensional phase diagram (a).

interactions (e.g. nanosystems with in-plane magnetization). However, in a large group of nanostructures with perpendicular anisotropy the magnetodipole coupling play an important role to stabilize specific multidomain patterns and topological defects^{15–19}. Generally in nanolayers and multilayers with perpendicular magnetization the stray fields can also strongly modify chiral patterns - helices and skyrmions²⁰. In this section I investigate the influence of long-range magnetostatic interactions on the characteristic features of isolated skyrmion states. It is only the first step to address the problem of the formation of the equilibrium modulated patterns under the competing influence of the Dzyaloshinskii-Moriya and magnetostatic interactions.

The total energy W of the skyrmion filament in the layer of thickness T can be written in the following reduced form:

$$\begin{aligned} \frac{WL_B}{2K_u} = & 2\pi T \int_0^\infty \left[\left(\frac{d\theta}{d\rho} \right)^2 + \frac{\sin^2 \theta}{\rho^2} + \sin^2 \theta + (2h - \frac{1}{Q})(1 - \cos \theta) + \right. \\ & \left. + \frac{4\chi}{\pi} \left(\frac{d\theta}{d\rho} + \frac{\sin \theta \cos \theta}{\rho} \right) - \frac{f(\rho)}{QT} \cos \theta \right] \rho d\rho \end{aligned} \quad (21)$$

where $L_B = \sqrt{A/K_u}$ serves as a scale of the non-dimensional radial variable ρ , and $Q = K_u/2\pi M^2$ is a quality factor,

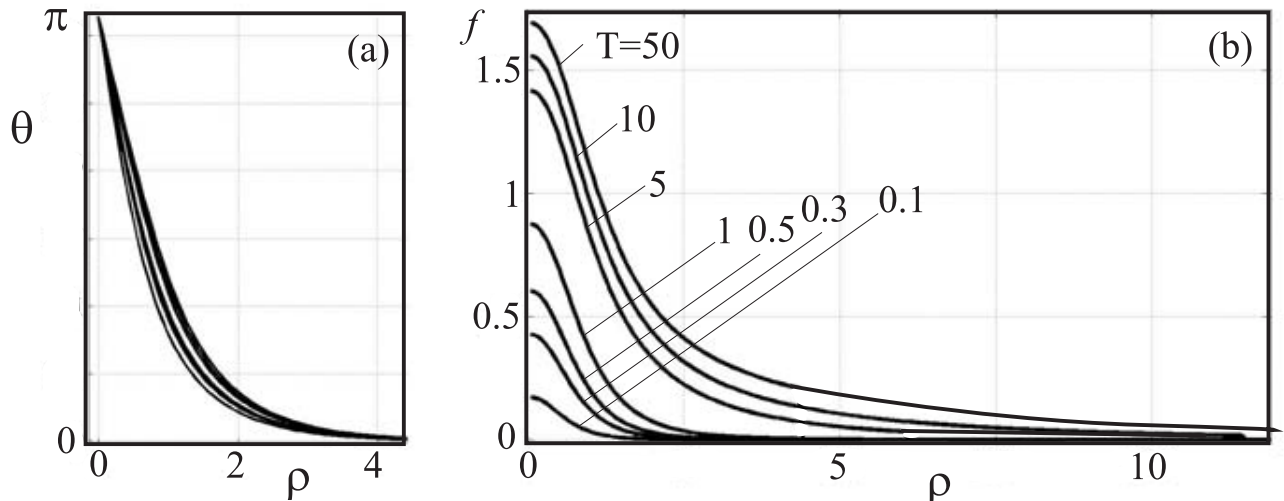


FIG. 4: (a) Equilibrium angular profiles $\theta(\rho)$ for skyrmion solutions of Eq. (21) plotted for different values of film thickness T , $h = -0.05$, $\varkappa = 0.5$, $Q = 5$; (b) function $f(\rho)$ (22) for corresponding skyrmion solutions.

$$\varkappa = \pi D / 4 \sqrt{AK_u}$$

The stray-field energy of the skyrmion string had been derived by solving the corresponding magnetostatic problem as shown in Ref.^{21,22} for magnetic bubble domains. Here, in Eq. (21)

$$f(\rho) = \int_0^\infty \int_0^\infty (1 - \cos \theta(\rho')) (1 - e^{-\xi T}) J_0[\xi \rho'] J_0[\xi \rho] \rho' d\rho' d\xi \quad (22)$$

J_0 is a Bessel function of zero order.

I solve the magnetostatic problem for two types of localized solutions (Fig. 4.14 (a), (e)). In the absence of demagnetizing fields the first localized solution (Fig. 4.14 (a)) represents skyrmion stabilized by the DM interactions. The second type of localized solution (Fig. 4.14 (e)) is unstable and can exist only in the field applied along the magnetization in the center. In the presence of dipole-dipole interactions this second type of the localized solution becomes stable, it is the solution for the famous magnetic bubble domain²⁰.

Typical solutions $\theta(\rho)$ for localized skyrmions are shown in Fig. 4. For quality factor $Q = 5$ and $\varkappa = 0.5$ I plot the set of solutions parametrized by the film thickness T . With the decrease of the thickness the angular profiles become more localized. The solutions for skyrmions can exist in very strong positive field: they are protected from the collapse by DM interaction.

Solutions for magnetic bubble domains shown in Fig. 5 are characterized by much larger radial sizes in comparison with skyrmions. Such solutions are stable only in the narrow interval of magnetic field applied against the magnetization in the center. Any slight deviation of the control parameters T , \varkappa , Q , and h leads to the instability of these magnetic domains, although as a solution of the Euler equation bubble domains can exist even in the absence of dipole-dipole interaction (as it is seen from Fig. 4.14 (e)-(h)).

Bubble domains and skyrmions are two fundamentally different types of solutions of micromagnetic functional. As bubble domains are stabilized only in the narrow region of applied magnetic fields and film thicknesses²³, the skyrmions look more preferable for the possible applications.

VII. OBSERVATIONS OF SKYRMIONIC AND HELICAL TEXTURES IN $\text{Fe}_{0.5}\text{Co}_{0.5}\text{Si}$ NANOLAYERS: THEORETICAL ANALYSIS

Real-space images of skyrmion states in a thin layer of cubic helimagnet $\text{Fe}_{0.5}\text{Co}_{0.5}\text{Si}$ have recently been obtained by using Lorentz transmission electron microscopy²⁴. This is the first clear experimental manifestation of *chiral skyrmion states* in a non-centrosymmetric magnetic crystal. The first-order transition of a helicoid into a skyrmion lattice and its subsequent transformation into a system of isolated skyrmions observed in bias magnetic fields (Figs. 1, d-f, 2, 3 (a-d) in²⁴) are in excellent agreement with the theoretical predictions on the behavior of skyrmions and

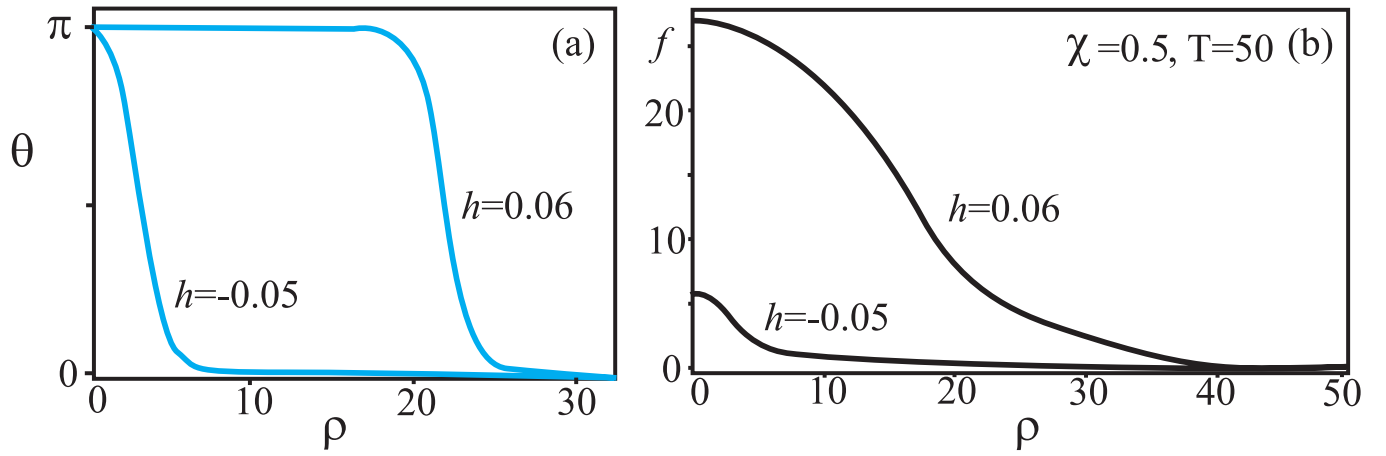


FIG. 5: (a) Equilibrium angular profiles $\theta(\rho)$ for magnetic bubble domains (Eq. (21)) plotted for $h = -0.05$ and $h = 0.06$, and $\chi = 0.5, Q = 5$; (b) function $f(\rho)$ (22).

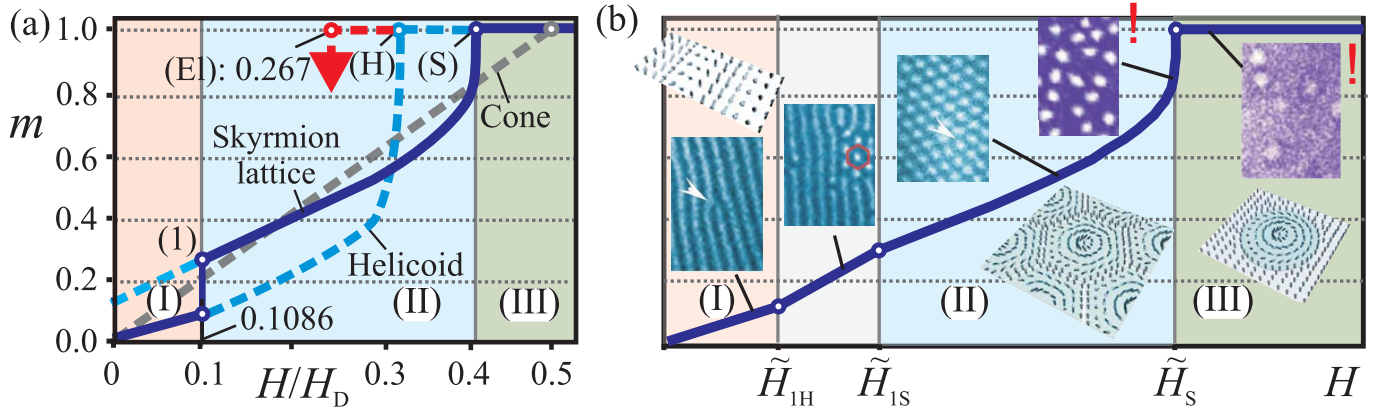


FIG. 6: The ideal magnetization curves for a bulk sample (based on results of¹²) (a) and for a thin layer (b) of a cubic helimagnet with suppressed cone phases. Solid lines indicate the thermodynamically stable states; dashed lines in Fig. (a), metastable configurations. The transition field H_1 in the thin layer "spreads" into a region of multidomain states. Fragments of experimentally observed images²⁴ demonstrate excellent agreement with theoretically calculated magnetization curves. The patterns indicated with sign (!) contain images of isolated chiral skyrmions.

the field-driven transitions into densely packed skyrmion lattices according to the magnetic phase diagrams calculated earlier^{12,25} (Fig. 6).

In the experiments, the thickness 20 nm of the magnetic layer $\text{Fe}_{0.5}\text{Co}_{0.5}\text{Si}$ is much smaller than the helix period $L_D = 90$ nm²⁴. But, even for such a small thickness, the conical state propagating only for a fraction of a period perpendicularly through the layer has lower energy than a skyrmion lattice, absent additional effects that stabilize it in applied fields. Usually in magnetic nanolayers strong perpendicular uniaxial anisotropy arises, either as a result of surface effects²⁶ or of lattice strains. Thus, induced anisotropies give a possible explanation for the experimental observation of the skyrmions in these $\text{Fe}_{0.5}\text{Co}_{0.5}\text{Si}$ layers, in accordance with the phase diagram for cubic helimagnets with uniaxial distortions [XI].

Fig. 6 presents the magnetization curve for a bulk isotropic helimagnet (a) (based on results of¹², Fig. 12) and the corresponding magnetization curve for a thin layer involving demagnetization effects²³ (b). Compared to theoretically calculated values in a bulk material (H_S, H_H) the corresponding critical fields in a thin layer are shifted, and their values can be estimated as $\tilde{H}_{S(H)} = H_{S(H)} + 4\pi M$. Due to demagnetization effects multidomain states can be stabilized in the vicinity of the transition field H_1 ¹². The boundaries of these regions with coexisting phases can be estimated as $\tilde{H}_{1H} = H_1 + 4\pi M m_H(H_1)$, $\tilde{H}_{1S} = H_1 + 4\pi M m_S(H_1)$. The magnetizations of the competing phases at the transition field equal $m_H(H_1) = 0.111$ and $m_S(H_1) = 0.278$. The jump of the magnetization at the transition equals $\Delta M = [m_S(H_1) - m_H(H_1)]M = 0.167M$, i.e., it reaches about 17 % of the saturation value.

The magnetization curves in Fig. 6 are constructed for ideally soft magnetic material under the condition that only the equilibrium states are realized in the magnetic sample. In real materials the formation of the equilibrium states is often hindered (especially during the phase transitions), and evolution of metastable states and hysteresis effects play an important role in the magnetization processes. Particularly, the formation of the skyrmion lattice below H_S can be suppressed. Then isolated skyrmions exist below this critical field. At a critical field H_{El} the skyrmions become unstable with respect to elliptical deformations and "strip-out" into isolated 2π domain walls. In a bulk material $H_{El} = 0.267 H_D$ (indicated in Fig. 6 with a red arrow). In a thin layer, one estimates $\tilde{H}_{El} = H_{El} + 4\pi M$. As discussed earlier^{12,25,27} the evolution of chiral skyrmions in magnetic fields has many features in common with that of bubble domains in perpendicular magnetized films,²³ and with Abrikosov vortices in superconductors²⁸.

The images from Ref.²⁴ (Fig.6 (b)) reflect in details theoretically predicted evolution of the chiral modulations in the applied magnetic field: the helicoid phase is realized at low fields (region (I)); at higher field this transforms into the skyrmion lattice (region (II)) via an intermediate state ($\tilde{H}_{1H} < H < \tilde{H}_{1S}$); finally the skyrmion lattice by extension of the period transforms into the homogeneous phase where isolated skyrmions still exist as topologically stable 2D solitons.

Two patterns indicated in Fig. 6 (b) with exclamation mark manifest the main result of Ref.²⁴: the first images of *static two-dimensional localized states* aka *chiral skyrmions*! In Ref.²⁴ this result has been overlooked and misinterpreted as a coexisting ferromagnetic and skyrmion lattice phases. As it was expounded in the previous section, the transition of the skyrmion lattice into the homogeneous state is a *continuous* transition, but of the particular *nucleation* type. Such transitions exclude the formation of coexisting states.

The condensed skyrmion phases in the micrograph of Ref.²⁴ also appear as heavily distorted densely packed two-dimensional lattice configurations. This is expected for skyrmionic matter. As these mesophases are composed from elastically coupled radial strings, dense skyrmion configurations generally do not form ideal crystalline lattices but various kinds of partially ordered states, e.g. hexatic ordering implying only orientational order of bonds without positional long-range order, or other glassy arrangement following standard arguments put forth for the similar vortex matter in type-II superconductors²⁸. The observation derives from the particle-like (or string-like) nature of skyrmions and suggests that skyrmionic mesophases may display rich phase diagrams.

VIII. OBSERVATION OF SKYRMION STATES IN CHIRAL LIQUID CRYSTALS

As it was noted in section II, the phenomenological energy of cholesterics (5) has an identical mathematical form as that of cubic helimagnets. This implies close relations between chiral textures in both condensed matter systems. However, in contrast to magnetic systems favoring smooth distributions of the order parameter, liquid crystals usually form patterns composed of various types of singularities. Defects in liquid crystals are of various dimensionalities, not only line defects, but also points and walls, and appear due to the prevalence of orientational order over positional in the applied magnetic or electric fields. In the defects the director \mathbf{n} is said to be undefined and the properties of defects are often not well controlled. For many years the investigations of liquid crystal textures have been mostly concentrated on the processes related to the formation and evolution of these topological defects^{8,29,30}. Only during the last decade physical analogies between liquid crystal and magnetic systems have been utilized to find new skyrmionic textures in these systems^{10,25,31,32}. Particularly, the analogy with cholesteric blue phases³⁰ has been used to establish the skyrmionic ground state in chiral magnetic metals near the ordering temperature²⁵. The results on observations of specific skyrmion states (spherulitics) in confined cholesteric systems (Fig. 7 (b))⁸ can help to investigate similar structures in magnetic nanolayers^{24,33}. Liquid crystals have several advantages over magnetic systems for the modelling and investigation of various inhomogeneous structures. The system parameters can be varied over wide limits to establish necessary conditions for a given experiment; as a rule experiments are conducted at room temperature and are comparatively simple; the results of investigations are easily visualized, to a degree not usually attainable in the investigation of magnetic nanolayers.

Fig. 7 shows modulated patterns in chiral magnets (c,d) in comparison with those in chiral liquid crystals (a,b). Under non-restricted conditions, chiral-nematic LC molecules, which are characterized by an antisymmetric center in the molecule, organize themselves by following a helicoidal director alignment (Fig. 7 (a)). However, more exotic ground states are possible (for example, cholesteric fingers³⁴ and/or triple-twist torons³⁵), in particular, spherulites (Fig. 7 (b)).

Such circular objects, called bubble domains or spherulites, can be formed as isolated entities or arranged in a hexagonal array (Fig. 7 (b)). For the first time, they have been observed in 1974 simultaneously by Kawachi and Kogure³⁶ and Haas and Adams³⁷ in materials of negative dielectric anisotropy. The spherulites were generated by applying pulses of DC or AC low frequency electric field strong enough to induce electrodynamic turbulence. Two years later, Bhide et al.³⁸ studied the optical properties of this pattern by laser diffraction and proposed that the bubble domain was a cholesteric pocket with oblate spheroid shape. This model was replaced by a more convincing

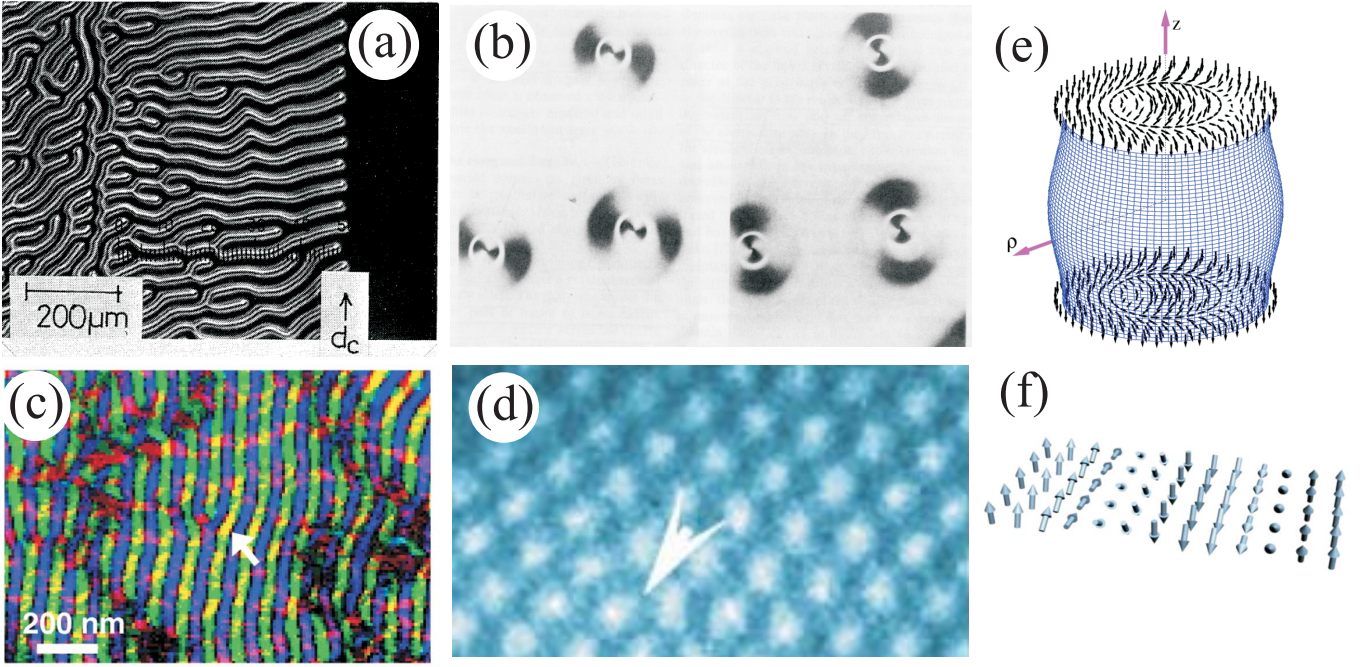


FIG. 7: Modulated phases in liquid crystals (a),(b) and their analogues in magnetic systems (c),(d): (a), (c) helical modulations in cholesterics⁸ and in cubic helimagnets⁴⁴ with the distribution of the order parameters shown as a sketch in (f); (b), (d) isolated spherulites in a chiral liquid crystal⁴² and hexagonal lattice of chiral skyrmions in $(\text{Fe,Co})\text{Si}^{24}$. (e) shows schematically the structure of a spherulite.

model in papers of Akahane et al.^{39,40}. In this model which was inspired by the paper of Cladis and Kleman⁴¹, two looped disclinations were assumed to exist near the glass plates. Another model of Stieb⁴² suggested that only one singular line is located along the axis of spherulite (Fig. 7 (b)). As well, according to the experiments of Pirkl et al.⁴³ the bubble domains can be formed from the looped finger in the cholesterics with positive dielectric anisotropy. In the present chapter I have shown that a non-singular model with a continuous distribution of the director field in the spherulite is among the solutions of the equations minimizing the Frank functional for the cholesteric layer with the homeotropic boundary alignment. Thus, the spherulitic bubbles in anchored chiral liquid crystal films^{36–38} may be skyrmion textures.

IX. CONCLUSIONS

In this chapter I investigated some effects imposed by the confined geometry of magnetic nanolayers on skyrmion states, namely, the influence of surface-induced anisotropy and demagnetizing fields on the stability and the structure of localized skyrmions. I showed that the surface-induced anisotropy produces pinning (anchoring) effect on magnetic states. It suppresses very effectively modulated skyrmion states and distorts the tubular structure of skyrmion filaments making them of convex-like shape with narrow "necks" near the surface. The similarity of phenomenological models for nonsingular spherulitics in liquid crystals and skyrmions in chiral magnetic materials offers new prospects for investigations of these solitonic states within a common theoretical approach. The rich experimental material on observation of spherulitic patterns in liquid crystals⁸ in this sense can be used as guidelines for investigations of skyrmion states in chiral magnetic layer systems.

Also in this section I addressed the problem of the influence of demagnetizing effects on the skyrmion solutions. I showed that skyrmions and magnetic bubble domains are two different branches of cylindrical magnetization structure with different mechanism of internal stabilization.

* Electronic address: leon-off@mail.ru

- ¹ Yu. M. Koroteev, G. Bihlmayer, J. E. Gayone, E. V. Chulkov, S. Blügel, P. M. Echenique, Ph. Hofmann, Phys. Rev. Lett. **93**, 046403 (2004).
- ² T. Hirahara, T. Nagao, I. Matsuda, G. Bihlmayer, E. V. Chulkov, Yu. M. Koroteev, P. M. Echenique, M. Saito, S. Hasegawa, Phys. Rev. Lett. **97**, 146803 (2006).
- ³ A. N. Bogdanov, U. K. Röbner, Phys. Rev. Lett. **87**, 037203 (2001).
- ⁴ M. Bode, M. Heide, K. von Bergmann, P. Ferriani *et al.*, Nature **447**, 190 (2007).
- ⁵ A. N. Bogdanov, U. K. Röbner, K.-H. Müller, J. Magn. Magn. Mater. **238**, 155 (2002).
- ⁶ L. Néel, J. Phys. Rad. **15**, 225 (1954).
- ⁷ A. N. Bogdanov, U. K. Röbner, arxiv: 0101262 (2001).
- ⁸ P. Oswald, J. Baudry, and S. Parkl, Phys. Rep. **337**, 67 (2000).
- ⁹ P. G. De Gennes and J. Prost, *The Physics of Liquid Crystals* (Oxford University Press, Oxford, 1993), 2nd ed.
- ¹⁰ A. N. Bogdanov, JETP Lett., **71**, 85 (2000).
- ¹¹ W. H. Press, S. A. Teukolsky, W. T. Vetterling, B. P. Flannery, *Numerical Recipes - The Art of Scientific Computing* (Cambridge University Press, Cambridge, 2007), 3d ed.
- ¹² A. Bogdanov, A. Hubert, J. Magn. Magn. Mater. **138**, 255 (1994).
- ¹³ E. H. Brandt, Phys. Rev. B **68**, 054506 (2003).
- ¹⁴ A. Bogdanov, A. Hubert, J. Magn. Magn. Mater. **195**, 182 (1999).
- ¹⁵ N. S. Kiselev, I. E. Dragunov, U. K. Röbner, A.N. Bogdanov, Appl. Phys. Lett. **91**, 132507 (2007).
- ¹⁶ N. S. Kiselev, U. K. Röbner, A.N. Bogdanov, O. Hellwig, Appl. Phys. Lett. **93**, 162502 (2008).
- ¹⁷ O. Hellwig, A. Berger, J. B. Kortright, E. E. Fullerton, J. Magn. Magn. Matter. **319**, 13 (2007).
- ¹⁸ C. Bran, A. B. Butenko, N. S. Kiselev, U. Wolff, L. Schultz, O. Hellwig, U. K. Röbner, A.N. Bogdanov, V. Neu, Phys. Rev. B **79**, 024430 (2009).
- ¹⁹ N. S. Kiselev, I. E. Dragunov, V. Neu, U. K. Röbner, A. N. Bogdanov J. Appl. Phys. **103**, 043907 (2008).
- ²⁰ N. S. Kiselev, A. N. Bogdanov, R. Schäfer, and U. K. Röbner, arXiv: 1102.2726v1 (2011).
- ²¹ Y. S. Lin, Y. O. Tu, Appl. Phys. Lett. **18**, 247 (1971).
- ²² Y. O. Tu, J. of Appl. Phys. **42**, 5704 (1971).
- ²³ A. Hubert, R. Schäfer, *Magnetic Domains* (Springer, Berlin 1998).
- ²⁴ X. Z. Yu, Y. Onose, N. Kanazawa *et al.*, Nature, **465**, 901 (2010).
- ²⁵ U. K. Röbner, A. N. Bogdanov, C. Pfeleiderer, Nature **442**, 797 (2006).
- ²⁶ M. T. Johnson, P. J. H. Bloemen, F. J. A. den Broeder, J. J. de Vries, Rep. Prog. Phys. **59**, 1409 (1996).
- ²⁷ A. N. Bogdanov and D. A. Yablonsky, Zh. Eksp. Teor. Fiz. **95**, 178 (1989) [Sov. Phys. JETP **68**, 101 (1989)].
- ²⁸ G. Blatter, M. V. Feigelman, V. B. Geshkenbein *et al.*, Rev. Mod. Phys. **66**, 1125 (1994).
- ²⁹ D. C Wright, N. D. Mermin, Rev. Mod. Phys. **61**, 385 (1989).
- ³⁰ R. M. Hornreich, M. Kugler, S. Shtrikman, Phys. Rev. Lett. **48**, 1404 (1982).
- ³¹ A. N. Bogdanov, U. K. Röbner, A. A. Shestakov, Phys. Rev. E, **87**, 016602 (2003).
- ³² A. N. Bogdanov, A. A. Shestakov, J. of Exp. and Theor. Phys. **86**, 911 (1998).
- ³³ X. Z. Yu, N. Kanazawa, Y. Onose *et al.*, Nature Mater. **10**, 106 (2011).
- ³⁴ I. I. Smalyukh *et al.*, Phys. Rev. E, **72**, 061707 (2005).
- ³⁵ I. I. Smalyukh, Y. Lansac, N. A. Clark, and R. P. Trivedi, Nature Mater. **9**, 139 (2009).
- ³⁶ M. Kawachi, O. Kogure, Y. Kato, Jap. J. Appl. Phys. **13**, 1457 (1974).
- ³⁷ W. E. L. Haas, J. E. Adams, Appl. Phys. Lett. **25**, 263 (1974); Appl. Phys. Lett. **25**, 535 (1974).
- ³⁸ V. G. Bhide, S. Chandra, S. C. Jain, R. K. Medhekar, J. of Appl. Phys. **47**, 120 (1976).
- ³⁹ T. Akahane, T. Tako, Molec. Crystals liq. Crystals, **38**, 251 (1977).
- ⁴⁰ S. Hirata, T. Akahane, and T. Tako, Molec. Crystals liq. Crystals, **75**, 47 (1981).
- ⁴¹ P. E. Cladis, M. Kleman, Molec. Crystals liq. Crystals, **16**, 1 (1972).
- ⁴² A. Stieb, J. Phys. France, **41**, 961 (1980).
- ⁴³ S. Pirkel, P. Ribiere, P. Oswald, Liq. Cryst. **13**, 413 (1993).
- ⁴⁴ M. Uchida *et al.*, Phys. Rev. B **77**, 184402 (2008).
- ⁴⁵ P. Bak and M. H. Jensen, J. Phys. C: Solid State Phys. **13**, L881 (1980).
- ⁴⁶ A. N. Bogdanov, U. K. Röbner, K.-H. Müller, J. Magn. Magn. Mat., **238**, 155 (2002).
- ⁴⁷ I. E. Dzyaloshinskii, J. Sov. Phys. JETP-USSR **19**, 960 (1964).